


# Development and Characterization of $\text{PbI}_2$ Nanoparticles for all Solid-State Flexible Supercapacitor Purposes

Gabriel de Souza Augusto<sup>a</sup>, Thomaz Amaral Oliveira<sup>b</sup>, Gabriel de Moraes Moura<sup>a</sup>,

Camila Cristina da Silva<sup>a</sup>, José Fernando Condeles<sup>b</sup>, Jeferson Aparecido Moreto<sup>b\*</sup> ,

Paulo Roberto de Oliveira<sup>a</sup>, Marcelo Mulato<sup>c</sup>, Rogério Valentim Gelamo<sup>a</sup>

<sup>a</sup>Instituto de Ciências Exatas e Tecnológicas, Universidade Federal do Triângulo Mineiro, Avenida Doutor Randolfo Borges Júnior, Univerdecidade, 38064200, Uberaba, MG, Brasil

<sup>b</sup>Instituto de Ciências Exatas, Naturais e Educação, Universidade Federal do Triângulo Mineiro, Avenida Doutor Randolfo Borges Júnior, Univerdecidade, 38064200, Uberaba, MG, Brasil

<sup>c</sup>Departamento de Física, Faculdade de Filosofia, Ciências e Letras, Universidade de São Paulo, Av. Bandeirantes, 3900, 14040-901, Ribeirão Preto, SP, Brasil

Received: December 09, 2018; Revised: March 20, 2019; Accepted: April 08, 2019

The development and utilization of new energy sources has been extensively studied in the world. Here, we report the development of flexible self-supported metal-free electrodes based on non-oxidized graphene multilayer (MLG) paper containing the lead iodide nanoparticles ( $\text{PbI}_2$ -NPs). The  $\text{PbI}_2$ -NPs was obtained and characterized by X-ray diffraction (XRD) and Raman spectroscopy. Supercapacitor containing the  $\text{PbI}_2$ -NPs in MLG electrodes was fabricated by a simple method and characterized using atomic force microscopy (AFM), cyclic voltammetry (CV) and galvanostatic charge-discharge techniques. The results show a flexible supercapacitor fashion reaching capacitance values of 154 F/g with high prospects in electronic area. Energy and power densities obtained for the pure MLG supercapacitor were  $3.40 \mu\text{Wh cm}^{-2}$  and  $0.73 \text{ mW cm}^{-2}$ , respectively. Regarding to  $\text{PbI}_2$ -NPs/MLG capacitor the energy and power density obtained were  $3.50 \text{ Wh kg}^{-1}$  and  $1.10 \text{ kW kg}^{-1}$ . The results herein presented open the possibility to new energy storage devices using  $\text{PbI}_2$ -NPs and MLG flexible supercapacitor configuration.

**Keywords:**  $\text{PbI}_2$ , Graphene, EDLC, Gel Electrolyte, Self-Standing, All-Solid-State Supercapacitor.

## 1. Introduction

In recent years, the development of alternative energy sources has become increasingly relevant<sup>1,2</sup>, both in respect to improved energy efficiency<sup>2</sup>, as a result of the rapid growth of portable electronic devices consumption, for example, as also for view of the development of environmentally friendly energy sources<sup>3</sup>. The electrochemical supercapacitors, also known as electrochemical double-layer capacitors (EDLC) or ultracapacitors<sup>4</sup> may be used as storage energy and has a longer life cycle compared to batteries for example (> 100 times life time), require a simple charging circuit, present no memory effect, are generally safe and they are low cost energy generators<sup>5</sup>.

In general, three types of materials are used in the supercapacitors construction: metal oxide<sup>6,7</sup>, conducting polymers<sup>8,9</sup> and carbonaceous materials. The most widely used are carbonaceous materials due to the variety of carbon-based materials that allows the possibility of construction of a wide range of carbon-based supercapacitors such as activated carbon<sup>10</sup>, carbon nanotubes (CNT)<sup>11</sup> and graphene<sup>12,13</sup>. With respect to polymers and metal oxides, the carbon-based materials have the advantage of presenting high stability

during the charge/discharge cycling<sup>12</sup>. Graphene-based materials have advantages over other carbon-based materials, as the CNT and activated carbon, for example. One of these advantages is its larger electrical double-layer capacitance<sup>12</sup>. In addition, graphene is a nanostructured material, such as CNT, with a high surface area. The large surface area promotes an increase in the efficiency of the supercapacitors with respect to capacitance and overall conductivity, improving the efficiency of the device<sup>5</sup>.

An application example of graphene-based materials as electrochemical supercapacitors is the use of graphene in the construction of flexible electrochemical supercapacitors<sup>14</sup>. Augusto *et. al.*<sup>15</sup> developed a flexible and self-standing solid-state supercapacitor using multilayer graphene paper (MLG) electrodes, which presented specific capacitances up to  $58,000 \mu\text{F cm}^{-2}$ . The capacitance of this device was further improved (practically twice) by the incorporation of polyaniline (PAni), a conductive film. By the incorporation of this polymer there is the sum of the pseudo-capacitance mechanism (conducting polymer) to the electrical double-layer capacitance (carbon-based materials), thus resulting in a hybrid supercapacitor<sup>12,15</sup>.

Metal oxide nanoparticles (NPs) can be excellent modifiers in doping of materials in the development of

\*e-mail: [jeferson.moreto.uftm@gmail.com](mailto:jeferson.moreto.uftm@gmail.com)

hybrid supercapacitors<sup>16,17</sup>. Lead iodide NPs ( $\text{PbI}_2$ -NPs) have been extensively developed due to their potential technological applications in active matrix flat panel imagers (AMFPI), room temperature ionizing radiation detectors, photo-detectors and photovoltaic cells.  $\text{PbI}_2$  presents a lamellar structure (I-Pb-I) and exhibits a large number of polytypes due to periodic stacking order alternation in the direction of the c-axis. The two most common polytypes are 2H- $\text{PbI}_2$  and 4H- $\text{PbI}_2$ . The forces within a lamellar structure between anion and cation layers are ionic, whereas the iodine-iodine interactions are weak (Van der Waal's interactions).  $\text{PbI}_2$  presents large band-gap (~2.3 eV), high mass density, high atomic number, high X-ray and  $\gamma$ -ray photon absorption, high charge collection and low leakage current<sup>18,19</sup>. J. Burschka *et al*<sup>20</sup> and M. Ledinsky *et al*<sup>21</sup> have applied a solution of  $\text{PbI}_2$  in N,N-dimethylformamide (DMF) to insert  $\text{PbI}_2$  into the  $\text{TiO}_2$  nanopores as a route to high-performance perovskite-sensitized solar cells. On the other hand, polycrystalline  $\text{PbI}_2$  films were obtained by solution evaporation in a furnace using DMF as solvent, with an average growth rate above  $30 \text{ \AA s}^{-1}$ <sup>22</sup>. DMF organic solvent shows a larger solubility limit for  $\text{PbI}_2$  and it has a relatively high boiling point (153 °C) in relation to other solvents as water for example. For conventional hydrothermal and solvothermal techniques, the precursor formation occurs in a long period time. However, this can lead to the rise of broad particle size and shape distributions. According to P.W. Dunne *et al*<sup>23</sup> an alternative is the temporal separation of the nucleation and growth stages. The nucleation must effectively happen only once such that the critical nucleation threshold is transposed quickly. Rapid nucleation then relieves the supersaturation bringing the system to the metastable state which cannot form new nuclei. This leads to a narrow size distribution, limiting Ostwald ripening, whose nuclei grow almost exclusively by diffusion process.

The aim of this work was to develop flexible electrochemical supercapacitors obtained from non-oxidized graphene multilayer papers modified with  $\text{PbI}_2$ -NPs. For this purpose, an electrolyte gel is placed between two modified MLG separated by an ion permeable separator in which each electrode-electrolyte interface acts as a capacitor, leading to an electrochemical supercapacitor. The performance and behaviour of supercapacitors obtained were accessed by using cyclic voltammetry (CV) and galvanostatic charge-discharge techniques as well as the characterization of electrode and nanoparticles by X-ray diffractometry (XRD), Raman spectroscopy and atomic force microscopy (AFM).

## 2. Material & Methods

### 2.1. Synthesis of $\text{PbI}_2$ -NPs

In the present study,  $\text{PbI}_2$  powder produced by Aldrich (99.999% of purity) was dissolved in DMF without any

additives or stabilizers at 100 °C with concentration of  $200 \text{ mg mL}^{-1}$ . Petri dishes were covered with 15 mL of the prepared solution and introduced into a furnace with constant temperature, kept without significant deviation at 100 °C for a period of 20 min. The temperature was then increased from 100 °C up to 150 °C during 30 min. In this sense, isothermal nucleation and metastable growth steps performed  $\text{PbI}_2$ -NPs synthesis.  $\text{PbI}_2$  powder is dissociated with the formation of lead and iodine ions. The nucleation rate is related to the capacity of these ions to recombine into instable state. Thus, the number of nucleation seeds on the surface was kept high. Due to solvent vaporization, these ions recombine leaving behind  $\text{PbI}_2$ -NPs synthesized by nucleation and diffusion process.

### 2.2. $\text{PbI}_2$ -NPs characterization

$\text{PbI}_2$ -NPs structural properties were investigated using XRD and Raman scattering experiments. XRD experiments were performed using a  $\text{Cu K}_\alpha$  radiation (wavelength of 1.5406 Å) from a Siemens D5005 diffractometer system. The Bragg angle  $2\theta$  scanning was performed with a step of 0.02 degree from 10 degree up to 70 degree. Raman Scattering experiments were carried out at room temperature with illumination at 647.1 nm (lies well above the absorption edge of  $\text{PbI}_2$ ) from  $10 \text{ cm}^{-1}$  up to  $200 \text{ cm}^{-1}$ .

### 2.3. Supercapacitor assembling

The flexible and free standing  $\text{PbI}_2$ -NPs /MLG supercapacitors were constructed using an experimental procedure according to Augusto *et al*<sup>15</sup>. Figure 1 presents the schematic of supercapacitor assembly. Multilayer graphene powder (80 mg) previously prepared by thermal expansion and mechanical exfoliation<sup>24,25</sup> was pressed at  $20 \text{ kgf cm}^{-2}$  using a stainless steel mold (3 cm diameter) and used in order to obtain the flexible and metal free electrodes.  $\text{PbI}_2$ -NPs (previously dispersed in propanol 99.9%) were spread over the MLG electrodes. The electrode mass before and after the  $\text{PbI}_2$ -NPs insertion was measured resulting in 2 mg of nanoparticles per electrode. The electrolyte gel was prepared following the procedure described by Lie *et al*<sup>26</sup>. The preparation consists of 3 g of polyvinyl-alcohol (PVA) added to a solution of deionized water (30 mL) and sulfuric acid (3 g), heated at 85 °C and continuously stirred until the solution turns into a gel electrolyte. The capacitor separator is a polyester sheet, 130  $\mu\text{m}$ -thick. Using the same procedure described above, pure MLG supercapacitors were prepared in order to study the effect of  $\text{PbI}_2$ -NPs insertion in the devices capacitance.

### 2.4. Electrode and supercapacitor characterization

Cyclic voltammetry (CV) is one of the most reliable techniques used to study electrochemical capacitors since it provides detailed information about the electric double-

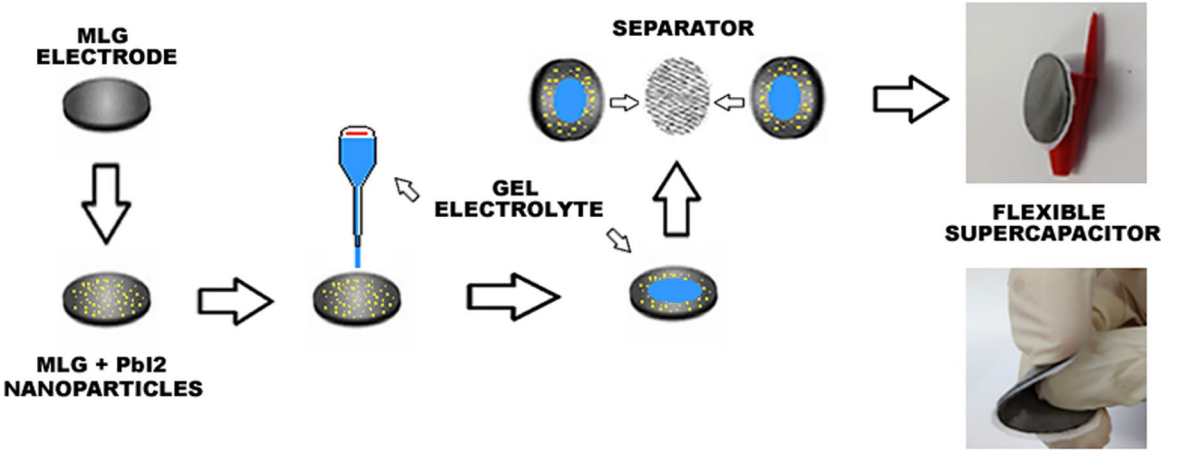


**Figure 1.** Schematic representation of supercapacitor assembly: PbI<sub>2</sub>-NPs were spread over MLG flexible electrodes and stacked with a polyester sheet separator between them, forming a flexible PbI<sub>2</sub>-NPs /MLG supercapacitor. The obtained supercapacitor has stretched and flexed form.

layer capacitance and its dependence with potential. The CV measurements were carried out at room temperature by using an Autolab model PGStat 302N potentiostat. For this purpose, six different scan rates from 0.005 to 0.2 V s<sup>-1</sup> were used in the electrochemical tests. All CV tests were done by using two electrodes configuration (reference electrode + counter electrode and - sensing electrode + working electrode) and more information about the experimental apparatus can be verified in Augusto *et al*<sup>15</sup>. The areal capacitance per electrode was calculated using equation 1:

$$C = 2 \frac{\int I dV}{\Delta V A \nu} \quad (1)$$

where I (A) is the electric current, A (cm<sup>2</sup>) the electrode area,  $\Delta V$  the voltage range and  $\nu$  the voltammetry scan rate<sup>27</sup>. It is important to mention that the area A can be exchanged for the electrode mass M for capacitance per mass estimative instead of capacitance per area resulting in specific capacitance. The capacitance C as a function of electrode area may be determined by using equation 2:

$$C = 2 \frac{I}{A \frac{dV}{dt}} \quad (2)$$

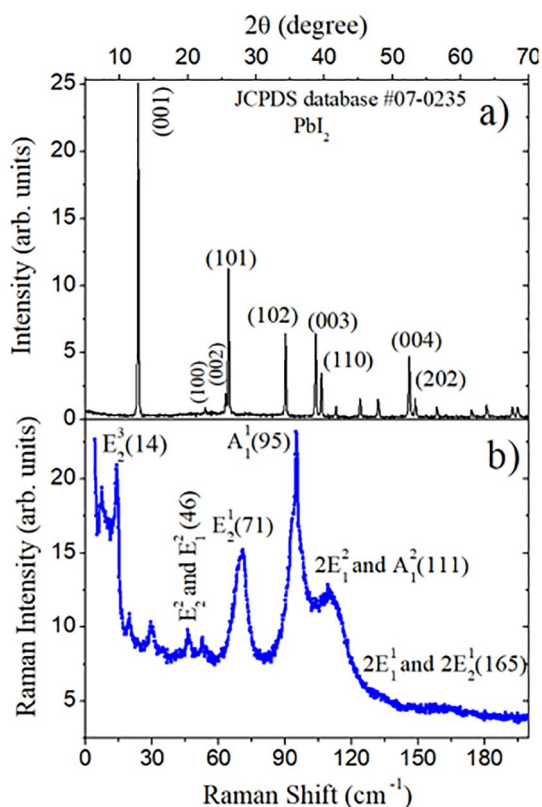
The capacitance C per electrode area was obtained from galvanostatic charge-discharge profiles<sup>28</sup>, according to the equation 2. Six different current densities from 0.008 A g<sup>-1</sup> to 0.039 A g<sup>-1</sup> (1.80 to 8.90 A m<sup>-2</sup>) were used in the galvanostatic cycles performed between 0.0 and 0.7 V. The  $dV/dt$  represents the slope of the discharge curve.

### 3. Results and Discussion

Figure 2 shows in (a) the X-ray diffraction (XRD) and in (b) the Raman scattering results for experiments performed with PbI<sub>2</sub>-NPs samples. The XRD data show that PbI<sub>2</sub>-NPs

are polycrystalline and preferentially oriented along the (001), (101), (102), (003), (110), and (004) directions that are related to 2H-PbI<sub>2</sub> polytype. These peaks confirm good crystallinity of NPs and were identified using the Joint Committee on Powder Diffraction Standards (JCPDS database number 07-0235). Note that the intensity of the (101) peak is 2.2 times as small as the one of the (001) peak. The highest intensity was observed along (001) direction which is in agreement with those single crystalline nanosheets obtained by microwave-assisted synthesis<sup>19</sup>. The NPs sizes were estimated to be about 43 nm, as determined using Debye-Scherrer equation and the full width at half-maximum (FWHM) of the most intense peak (001)<sup>29</sup>. The Raman modes are identified as  $E_2^3$  at 13.9 cm<sup>-1</sup>,  $E_2^1$  at 70.8 cm<sup>-1</sup>,  $A_1^1$  at 95.0 cm<sup>-1</sup> and  $A_1^2$  at 110.2 cm<sup>-1</sup>. Other modes of small intensities as  $E_1^1$  e  $E_2^2$  near 46 cm<sup>-1</sup> and  $2E_2^1$  near 165 cm<sup>-1</sup> were observed. The Raman-active  $A_1^1$  and  $A_1^2$  define the breathing motion of the PbI<sub>2</sub> layers. The Raman lines  $E_2^1$ ,  $E_2^2$ ,  $E_1^1$  and  $E_2^3$  correspond to the shear deformation modes and the three last modes are exclusive for 4H-PbI<sub>2</sub> polytype. The Raman vibration modes of PbI<sub>2</sub>-NPs are in agreement with 2H-PbI<sub>2</sub> polytype predominantly. However, are partially comparable with 4H polytype PbI<sub>2</sub> assignments due to  $E_2^2$ ,  $E_1^1$  and  $E_2^3$  modes. These 4H-PbI<sub>2</sub> exclusive modes can be attributed to a partial transformation to 4H polytype, which indicates stacking faults arrangements<sup>18</sup>. Stacking faults motions in PbI<sub>2</sub> are mainly induced by slither between contiguous anion-anion layers due to weak binding<sup>18</sup>.

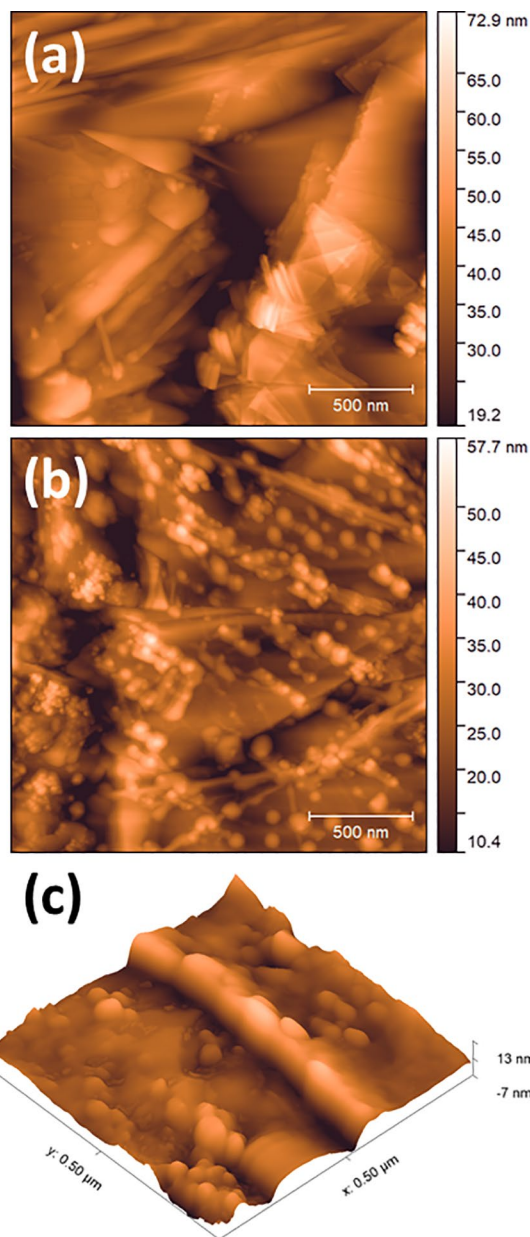
The electrodes morphology was evaluated by AFM microscopy in dynamic mode. The graphene borders and different planes overlapping can be seen and a free defective surface is observed in Figure 3A. The morphology of this MLG electrode is changed using PbI<sub>2</sub>-NPs over the surface according to Figure 3B. The PbI<sub>2</sub>-NPs present spherical morphology and regular distribution of particles over MLG



**Figure 2.** (a) X-ray diffraction and (b) Raman scattering spectra obtained from  $\text{PbI}_2$ -NPs.

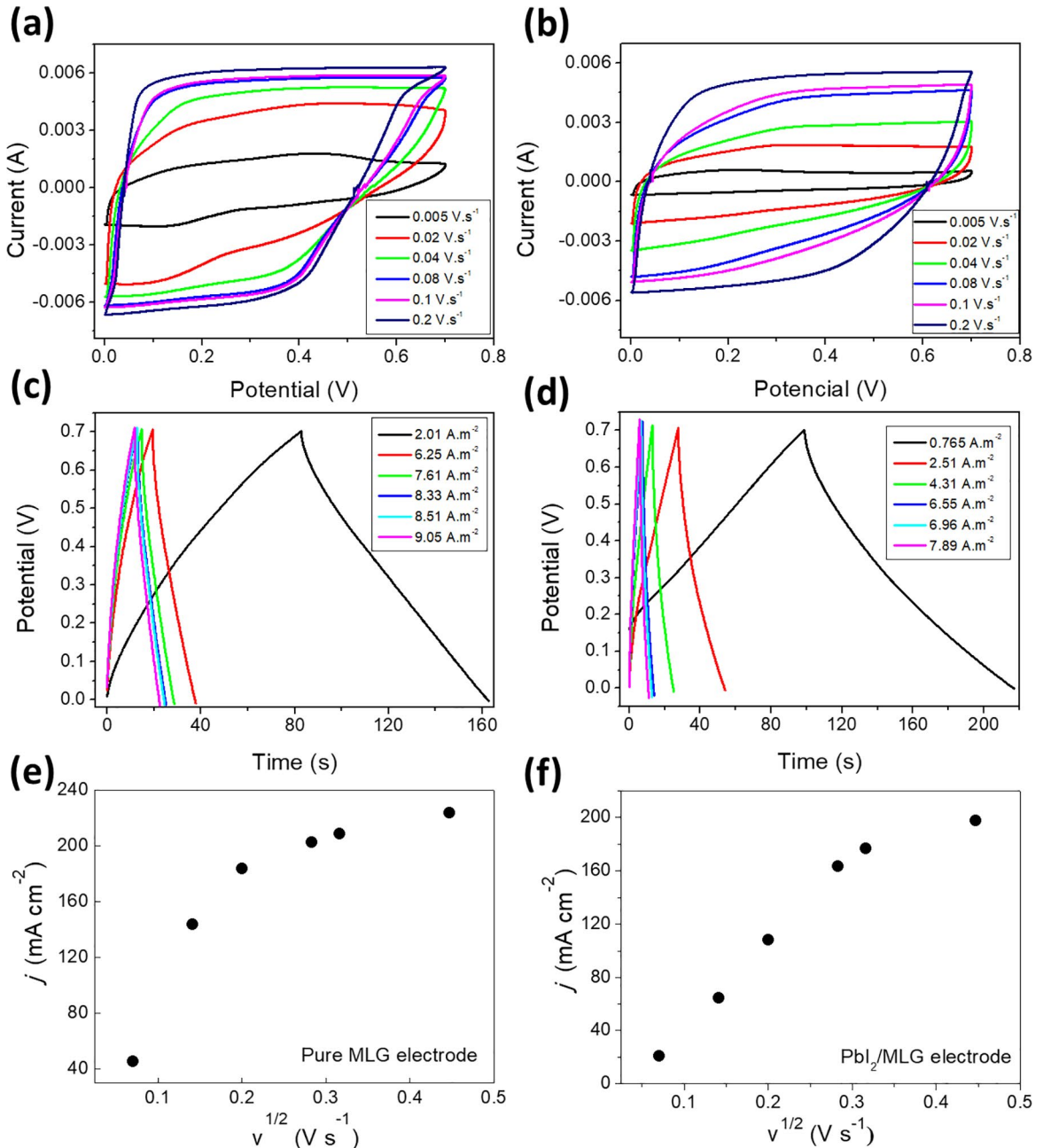
surface. The voids between MLG flakes in the electrode contribute to the permeation pores creation and consequent increase of the capacitance. Using a higher magnification ( $1 \mu\text{m}^2$ ) and the software Gwyddion, it was possible to obtain the nanoparticles mean size about  $35.5 \pm 3.5 \text{ nm}$ .

Figure 4 (a) exhibits stable electrochemical performance of the pure MLG and  $\text{PbI}_2$ -NPs/MLG supercapacitors obtained using CV technique at scan rates of 0.005, 0.02, 0.04, 0.08, 0.1 and  $0.2 \text{ V s}^{-1}$ . As can be seen in all voltammograms, the specific capacitance gradually decreased with increasing scanning rate, which is a typical behaviour expected for these systems and also observed in several other works of the literature<sup>26,30</sup>. Probably, the larger capacitance values at lower scanning rates are due to a higher adsorption of ions in the electric double layer. The shapes of the CV curves distinctly reveal the pseudocapacitive characteristics as well as electrolyte stability along the cycling. In the present work, the influence of the electrode construction parameters as compacting pressure and  $\text{PbI}_2$ /MLG mass was also analyzed. Both electrodes herein used (pure MLG and  $\text{PbI}_2$ -NPs/MLG) probably exhibited the electric double layer capacitance effect (DLCE) behaviour, since no redox reactions mechanism has occurred during the charge and discharge process (see Figures 4(a) and (b)) resulting in CV curve profile presenting rectangular shape and highly symmetric in nature without



**Figure 3.** (a) Atomic force microscopy images of pure MLG electrode pressed at  $20 \text{ kgf cm}^{-2}$ , (b)  $\text{PbI}_2$  nanoparticles over the MLG electrode and (c) 3D image of  $\text{PbI}_2$  nanoparticles using higher magnification.

significant deformation observed for carbon materials and other structures<sup>31,32</sup>. In fact, the flexible and metal free MLG electrode has been tested efficiently in flexible and all solid state supercapacitor<sup>15</sup>. Regarding the galvanostatic charge and discharge results, as can be seen in Figures 4 (c) and (d), it is possible to verify that a triangular and symmetric potential profiles were observed for all currents applied, reinforcing the DLCE characteristic of these supercapacitors as suggested in other works<sup>15,28,31,32</sup>. However, since the redox reactions resulting in pseudocapacitive behaviour can occur with no distortion or peaks presence in CV curves, its presence



**Figure 4.** (a) CV curves for different scan rates for Pure MLG supercapacitor, (b) CV curves for different scan rates for  $\text{PbI}_2$ -NPs/MLG supercapacitor, (c) Galvanostatic charge and discharge curves at different current densities for Pure MLG supercapacitor, (d) Galvanostatic charge and discharge curves at different current densities for  $\text{PbI}_2$ -NPs/MLG supercapacitor, (e) Current density versus scan rate for pure MLG supercapacitor and (f) Current density versus scan rate for  $\text{PbI}_2$ -NPs /MLG hybrid supercapacitor.

can be evaluated using the Randles-Sevcik equation<sup>32</sup> that result in a linear fit in plot of current density versus square root of the scan rate. As can be seen in Figure 4 (e) and (f) a non-linear and linear behaviour for pure MLG and  $\text{PbI}_2$ /MLG capacitor was obtained, respectively indicating some redox reactions when  $\text{PbI}_2$  nanoparticles were used. The non-linear behaviour at higher scan rates is generally found in porous structured material and is due to ohmic-drop

effects<sup>33</sup>. This effect occurs due to the difficulty of access to certain charge generating sites. With the presence of the nanoparticles, the Ohmic drop effect is practically null, since there is little deviation from the linearity. This suggests that the presence of the nanoparticles increases the mass transport to the charge generating sites, probably due to the reduced size of these particles, even at high potential scanning rates. The improvement of mass transport, when in the presence

of nanoparticulate material, is related to the contribution of mass transport of the radial rather than linear type, as explored in other works<sup>34</sup>.

The constant time increased about 55 s using  $\text{PbI}_2$ -NPs in the electrode. This increase can be originated in two main experimental parameters: i) electrode resistance or ii) circuit capacitance. The parameter (i) probably is affected by the semiconductor behaviour of the nanostructures resulting in a higher electrical resistance between the gel electrolyte and MLG electrode, decreasing the global capacitance while (ii) contributed directly with the capacitance increase. The capacitances obtained using equation 2 and the galvanostatic charge and discharge curves (Figure 4 (c) and (d)) were  $126.000 \mu\text{F cm}^{-2}$  and  $84.5 \text{ F g}^{-1}$ , for pure MLG and  $\text{PbI}_2$ -NPs/MLG supercapacitors, respectively.

The difference in performance according to the variation of these parameters can be seen in the specific capacitance values shown in Figure 5a. Given the difficulty to determine the MLG mass in direct contact with the electrolyte gel, it is more appropriate to express the capacitance per area (areal capacitance -  $\mu\text{F cm}^{-2}$ )<sup>28</sup>. Otherwise, the capacitance per mass (specific capacitance) is a better parameter for the case of  $\text{PbI}_2$ -NPs/MLG given  $\text{PbI}_2$ -NPs mass was previously determined. The MLG specific capacitance reached almost  $130.000 \mu\text{F cm}^{-2}$  consistent with the previously reported values for similar capacitor<sup>15</sup>. Considering the hybrid nanostructured electrode herein studied, the capacitance reached  $\sim 90 \text{ F g}^{-1}$  using about 4 mg of  $\text{PbI}_2$ -NPs over the pairs of electrodes (2 mg in each supercapacitor). Despite the use of nanostructures has led to high capacitance per mass (hundreds of  $\text{F g}^{-1}$ )<sup>15,30,35</sup>, the use of  $\text{PbI}_2$ -NPs can block the permeation of gel electrolyte and interfere in the charge diffusion in the electric double layer, resulting in a smaller capacitance<sup>36</sup> compared with the pure MLG supercapacitor. This effect is reinforced by the AFM image in Figure 3b, given the empty spaces between graphene flakes, considered as pores for the electrolyte gel permeation inside in the electrode, are partially filled with the nanoparticles of  $\text{PbI}_2$ . Thus, the NPs distribution and quantity over the MLG electrodes are parameters that should be considered and controlled in order to improve the device capacitance. However, some gel permeation over the MLG pores can occurred and the capacitor performance carries characteristics both carbon nanostructure as well as the  $\text{PbI}_2$  nanoparticles.

Energy and power densities equals to  $3.40 \mu\text{Wh cm}^{-2}$  and  $0.73 \text{ mW cm}^{-2}$  were obtained for the pure MLG supercapacitor and presented in Figure 5b (inset). Considering the mass for the  $\text{PbI}_2$ -NPs in the capacitor herein studied, the energy and power density obtained were  $3.50 \text{ Wh kg}^{-1}$  and  $1.10 \text{ kW kg}^{-1}$ , respectively. The excellent capacitive properties of MLG paper electrode contributed positively to obtain an electrochemically reliable and flexible platform for the study and application of several nanostructures in the field of electrical charge storage.

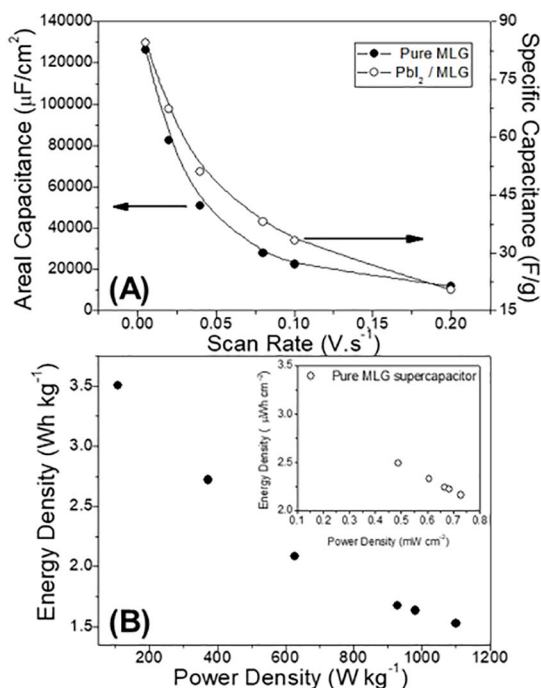


**Figure 5.** (a) Areal capacitance (capacitance per area unit) for Pure MLG supercapacitor versus scan rate (at left) and specific capacitance (per mass) versus scan rate for  $\text{PbI}_2$ -NPs/MLG supercapacitor (at right) and (b) Ragone plot for  $\text{PbI}_2$ -NPs/MLG supercapacitor and for pure MLG in inset. The lines linking the experimental points are only guide for eyes.

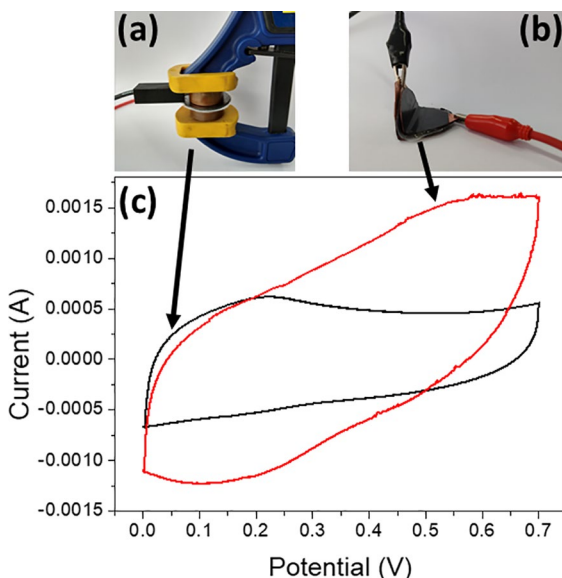


**Figure 6.** (a) Electrode setup for electrochemical characterization in line 0 angle, (b) in 90 degrees bend angle and (c) the CV curve at  $0.005 \text{ V.s}^{-1}$  at the 0 and 90 degrees configuration.

In order to show the flexibility of our device a comparison of the CV curves was made for the same  $\text{PbI}_2$ -NPs/MLG supercapacitor recorded at  $0.005 \text{ V s}^{-1}$  scan rate for 0 and 90 degrees, as presented in Figure 6. Surprisingly, at 90 degree a considerable increase in capacitance was observed

reaching 154 F g<sup>-1</sup> while ~90 F g<sup>-1</sup> was obtained for in line configuration. The reasons for that uninspected increase could be the higher gel diffusion in MLG pores, nanoparticle migration in interface gel/electrode or other instability related to the geometry change.

#### 4. Conclusions

PbI<sub>2</sub>-NPs were successfully synthesized in this work resulting in ~35 nm diameter polycrystalline material preferentially oriented along directions that are related to 2H-PbI<sub>2</sub> polytype. The Raman vibration modes of PbI<sub>2</sub>-NPs are in agreement with 2H-PbI<sub>2</sub> polytype predominantly, with a partial transformation to 4H polytype. The PbI<sub>2</sub>-NPs morphology evaluated by AFM, present a spherical shape and regular distribution of particles over MLG surface. The voids between MLG flakes in the electrode contribute to the permeation pores creation and consequent increase of the capacitance. Flexible and free-standing metal free supercapacitors were constructed and tested using PbI<sub>2</sub>-NPs/MLG electrodes. The CV and galvanostatic charge and discharge characterizations show the EDLC behaviour of pure MLG and PbI<sub>2</sub>-NPs/MLG supercapacitors. Capacitances were obtained in the order of about 126.000 μF cm<sup>-2</sup> for pure MLG supercapacitor and ~90 F g<sup>-1</sup> at 0 degree and ~154 F g<sup>-1</sup> bending at 90 degrees for PbI<sub>2</sub>-NPs/MLG supercapacitor. The energy and power density obtained for PbI<sub>2</sub>-NPs/MLG supercapacitor were 3.50 Wh kg<sup>-1</sup> and 1.10 kW kg<sup>-1</sup>, respectively. The MLG electrodes successfully performed as a base electrode for PbI<sub>2</sub>-NPs flexible supercapacitor. The results herein presented open the possibility to new energy storage devices using PbI<sub>2</sub>-NPs and MLG configuration.

#### 5. Acknowledgments

The authors would like to thank M. Hamsteiner from Paul Drude Institute in Berlin for Raman experiments. This work was partially supported by CNPq (Grant 402142/2016-0 and 303684/2015-1), Capes, Fapemig (Grant APQ-0227618) Brazilian agencies, National Institute of Science & Technology and Nacional de Grafite Ltda by the natural graphite donated and used in this work.

#### 6. References

- Barreto RA. Fossil fuels, alternative energy and economic growth. *Economic Modelling*. 2018;75:196-220. DOI: 10.1016/j.econmod.2018.06.019
- Miller JR. Perspective on electrochemical capacitor energy storage. *Applied Surface Science*. 2017;460:3-7. DOI: 10.1016/j.apsusc.2017.10.018
- Chu S, Majumdar A. Opportunities and challenges for a sustainable energy future. *Nature*. 2012;488:294-303. DOI: 10.1038/nature11475
- Pandolfo AG, Hollenkamp AF. Carbon properties and their role in supercapacitors. *Journal of Power Sources*. 2006;157(1):11-27. DOI: 10.1016/j.jpowsour.2006.02.065
- Aricò AS, Bruce P, Scrosati B, Tarascon JM, Van Schalkwijk W. Nanostructured materials for advanced energy conversion and storage devices. In: Dusastre V, ed. *Materials for Sustainable Energy*. London: Nature Publishing Group; 2010. p. 148-159. DOI: 10.1142/9789814317665\_0022
- Jiang J, Kucernak A. Electrochemical supercapacitor material based on manganese oxide: preparation and characterization. *Electrochimica Acta*. 2002;47(15):2381-2386. DOI: 10.1016/S0013-4686(02)00031-2
- Vishnu Prataap RK, Arunachalam R, Pavul Raj R, Mohan S, Peter L. Effect of electrodeposition modes on ruthenium oxide electrodes for supercapacitors. *Current Applied Physics*. 2018;18:1143-1148. DOI: 10.1016/j.cap.2018.06.015
- de Oliveira AHP, Nascimento MLF, de Oliveira HP. Carbon Nanotube@MnO<sub>2</sub>@Polypyrrole Composites: Chemical Synthesis, Characterization and Application in Supercapacitors. *Materials Research*. 2016;19(5):1080-1087. DOI: 10.1590/1980-5373-MR-2016-0347
- Na R, Lu N, Zhang S, Huo G, Yang Y, Zhang C, et al. Facile synthesis of a high-performance, fire-retardant organic gel polymer electrolyte for flexible solid-state supercapacitors. *Electrochimica Acta*. 2018;290:262-272. DOI: 10.1016/j.electacta.2018.09.074
- Rodrigues AC, da Silva EL, Quirino SF, Cuña A, Marcuzzo JS, Matsushima JT, et al. Ag@Activated Carbon Felt Composite as Electrode for Supercapacitors and a Study of Three Different Aqueous Electrolytes. *Materials Research*. 2019;22(1):e20180530. DOI: 10.1590/1980-5373-mr-2018-0530
- Kaempgen M, Chan CK, Ma J, Cui Y, Gruner G. Printable Thin Film Supercapacitors Using Single-Walled Carbon Nanotubes. *Nano Letters*. 2009;9(5):1872-1876. DOI: 10.1021/nl8038579
- Liu C, Yu Z, Neff D, Zhamu A, Jang BZ. Graphene-based supercapacitor with an ultrahigh energy density. *Nano Letters*. 2010;10(12):4863-4868. DOI: 10.1021/nl102661q
- Zhang LL, Zhou R, Zhao XS. Graphene-based materials as supercapacitor electrodes. *Journal of Materials Chemistry*. 2010;20(29):5983-5992. DOI: 10.1039/c000417K
- Wu ZK, Lin Z, Li L, Song B, Moon K, Bai SL, et al. Flexible micro-supercapacitor based on in-situ assembled graphene on metal template at room temperature. *Nano Energy*. 2014;10:222-228. DOI: 10.1016/j.nanoen.2014.09.019
- Augusto GS, Scarmínio J, Silva PRC, de Siervo A, Rout CS, Rouxinol F, et al. Flexible metal-free supercapacitors based on multilayer graphene electrodes. *Electrochimica Acta*. 2018;285:241-253. DOI: 10.1016/j.electacta.2018.07.223
- Cottineau T, Toupin M, Delahaye T, Brousse T, Bélanger D. Nanostructured transition metal oxides for aqueous hybrid electrochemical supercapacitors. *Applied Physics A*. 2006;82(4):599-606. DOI: 10.1007/s00339-005-3401-3
- Aghazadeh M, Karimzadeh I, Maragheh MG, Ganjali MR. Enhancing the Supercapacitive and Superparamagnetic Performances of Iron Oxide Nanoparticles through Yttrium Cations Electro-chemical Doping. *Materials Research*. 2018;21(5):e20180094. DOI: 10.1590/1980-5373-MR-2018-0094

18. Condeles JF, Mulato M. Crystalline texture and mammography energy range detection studies of pyrolysed lead iodide films: Effects of solution concentration. *Materials Chemistry and Physics*. 2015;166:190-195. DOI: 10.1016/j.materchemphys.2015.09.048
19. Shkir M, Yahia IS, Ganesh V, Bitla Y, Ashraf IM, Kaushik A, et al. A facile synthesis of Au-nanoparticles decorated PbI<sub>2</sub> single crystalline nanosheets for optoelectronic device applications. *Scientific Reports*. 2018;8:13806. DOI: 10.1038/s41598-018-32038-5
20. Burschka J, Pellet N, Moon SJ, Humphry-Baker R, Gao P, Nazeeruddin MK, et al. Sequential deposition as a route to high-performance perovskite-sensitized solar cells. *Nature*. 2013;499:316-319. DOI: 10.1038/nature12340
21. Ledinský M, Löper P, Niesen B, Holovský J, Moon SJ, Yum JH, et al. Raman Spectroscopy of Organic-Inorganic Halide Perovskites. *Journal of the Physical Chemistry Letters*. 2015;6(3):401-406. DOI: 10.1021/jz5026323
22. Condeles JF, Mulato M. Polycrystalline lead iodide films produced by solution evaporation and tested in the mammography X-ray energy range. *Journal of Physics and Chemistry of Solids*. 2016;89:39-44. DOI: 10.1016/j.jpcs.2015.10.012
23. Dunne PW, Munn AS, Starkey CL, Huddle TA, Lester EH. Continuous-flow hydrothermal synthesis for the production of inorganic nanomaterials. *Philosophical Transactions of the Royal Society A: Mathematical, Physical and Engineering Sciences*. 2015;373:20150015. DOI: 10.1098/rsta.2015.0015
24. Rouxinol FP, Gelamo RV, Amici RG, Vaz AR, Moshkalev SA. Low contact resistivity and strain in suspended multilayer graphene. *Applied Physics Letters*. 2010;97(25):253104. DOI: 10.1063/1.3528354
25. Machuno LGB, Oliveira AR, Furlan RH, Lima AB, Morais LC, Gelamo RV. Multilayer Graphene Films Obtained by Dip Coating Technique. *Materials Research*. 2015;18(4):775-780. DOI: 10.1590/1516-1439.005415
26. Liu L, Niu Z, Zhang L, Zhou W, Chen X, Xie S. Nanostructured Graphene Composite Papers For Highly Flexible And Foldable Supercapacitors. *Advanced Materials*. 2014;26:4855-4862. DOI: 10.1002/adma.201401513
27. Xu Y, Lin Z, Huang X, Liu Y, Huang Y, Duan X. Flexible Solid-State Supercapacitors Based on Three-Dimensional Graphene Hydrogel Films. *ACS Nano*. 2013;7(5):4042-4049. DOI: 10.1021/nn4000836
28. Yang C, Zhang L, Hu N, Yang Z, Wei H, Xu ZJ, et al. Densely-packed graphene/conducting polymer nanoparticle papers for high-volumetric-performance flexible all-solid-state supercapacitors. *Applied Surface Science*. 2016;379:206-212. DOI: 10.1016/j.apsusc.2016.04.058
29. Cullity BD. *Elements of X-Ray Diffraction*. 2nd ed. Reading: Addison-Wesley; 1978.
30. Sahoo S, Ratha S, Rout CS. Spinel NiCo<sub>2</sub>O<sub>4</sub> Nanorods for Supercapacitor Applications. *American Journal of Engineering and Applied Sciences*. 2015;8(3):371-379. DOI: 10.3844/ajeassp.2015.371.379
31. Simon P, Gogotsi Y. Materials for Electrochemical Capacitors. *Nature Materials*. 2008;7:845-854. DOI: 10.1038/nmat2297
32. Jadhav S, Kalubarme RS, Terashima C, Kale BB, Godbole V, Fujishima A, et al. Manganese dioxide/reduced graphene oxide composite an electrode material for high-performance solid state supercapacitor. *Electrochimica Acta*. 2019;299:34-44. DOI: 10.1016/j.electacta.2018.12.182
33. Grupioni AAF, Arashiro E, Lassali TAF. Voltammetric characterization of an iridium oxide-based system: the pseudocapacitive nature of the Ir<sub>0.3</sub>Mn<sub>0.7</sub>O<sub>2</sub> electrode. *Electrochimica Acta*. 2002;48(4):407-418. DOI: 10.1016/S0013-4686(02)00686-2
34. Lin C, Compton RG. Understanding mass transport influenced electrocatalysis at the nanoscale via numerical simulation. *Current Opinion in Electrochemistry*. 2018. In Press. DOI: 10.1016/j.coelec.2018.08.001
35. Xiong P, Huang H, Wang X. Design and synthesis of ternary cobalt ferrite/graphene/polyaniline hierarchical nanocomposites for high-performance supercapacitors. *Journal of Power Sources*. 2014;245:937-946. DOI: 10.1016/j.jpowsour.2013.07.064
36. Pendashteh A, Mousavi MF, Rahmanifar MS. Fabrication of anchored copper oxide nanoparticles on graphene oxide nanosheets via an electrostatic coprecipitation and its application as supercapacitor. *Electrochimica Acta*. 2013;88:347-357. DOI: 10.1016/j.electacta.2012.10.088